Clim Dyn
DOI 10.1007/s00382-007-0302-5

The impact of atmospheric nonlinearities on the fastest growth of ENSO prediction error

Xiaobing Zhou · Youmin Tang · Ziwang Deng

Received: 26 January 2007 / Accepted: 29 July 2007
© Springer-Verlag 2007

Abstract In this paper we explore the impact of atmospheric nonlinearities on the optimal growth of initial condition error of El Niño and the Southern Oscillation (ENSO) prediction using singular vector (SV) analysis. This is performed by comparing and analyzing SVs of two hybrid coupled models (HCMs), one composed of an intermediate complexity dynamical ocean model coupled with a linear statistical atmospheric model, and the other one with the same ocean model coupled with a nonlinear statistical atmosphere. Tangent linear and adjoint models for both HCMs are developed. SVs are computed under the initial conditions of seasonal background and actual ENSO cycle simulated by the ocean model forced with the real wind data of 1980–1999. The optimization periods of 3, 6 and 9 months are individually considered. The results show that the first SVs in both HCMs are very similar to each other, characterized by a central east-west dipole pattern spanning over the entire tropical Pacific. The spatial patterns of the leading SV in both HCMs are not sensitive to optimization periods and initial time. However, the first singular value, indicating the optimal growth rate of prediction error, displays considerable differences between the two HCMs, indicating a significant impact of atmospheric nonlinearities on the optimal growth of ENSO prediction error. These differences are greater with increasing optimization time, suggesting that the impact of atmospheric nonlinearities on the optimal growth of prediction error becomes larger for a longer period of prediction.

X. Zhou · Y. Tang (✉) · Z. Deng
Environmental Science and Engineering,
University of Northern British Columbia,
3333 University Way, Prince George,
BC, Canada V2N 4Z9
e-mail: ytang@unbc.ca

1 Introduction

In past three decades or so, the El Niño and the Southern Oscillation (ENSO) has received tremendous attention. While significant progress has been made in ENSO theories and predictions over years, especially through the TOGA (Tropical Ocean Global Atmosphere) program, the intrinsic mechanism of ENSO has been an issue of debate, i.e., is ENSO a linearly damped, stochastically driven dynamical system or is it a nonlinearly chaotic system? This central issue of ENSO has been an intensive research topic in last decades (e.g., Jin et al. 1994; Tziperman et al. 1994; Chen et al. 2004; Chang et al. 1996; Penland and Sardeshmukh 1995; Moore and Kleeman 1999; Thompson and Battisti 2001; Tang 2002; Tang et al. 2002, Eisenman et al. 2005; Gebbie et al. 2007). In past studies, both linear and nonlinear systems were successfully proposed to address some basic ENSO characteristics such as seasonal phase locking and oscillation irregularity.

An effective approach advancing the study of the regime of ENSO is to investigate the impact of atmospheric nonlinearities on the ENSO. It has been shown in some recent works that nonlinear nature of the atmosphere is important to understand the dynamical regime of ENSO (e.g., Jin et al. 2003; An and Jin 2004; Eisenman et al. 2005; Gebbie et al. 2007). Thus it is interesting to compare the ENSO nature and characteristics between two hybrid models, one composed of a dynamical ocean mode coupled to a nonlinear atmospheric model (NHCM) and the other coupled

the same ocean to a linear atmospheric model (LHCM). This was done in Tang et al. (2001), Tang (2002) and Tang and Hsieh (2002) where a nonlinear- and linear atmospheric model was, respectively, constructed using the neural network (NN) and linear regression (LR). In these works, the impact of atmospheric nonlinearities on the ENSO was explored through a forward diagnostic strategy, namely that the LHCM and the NHCM were integrated forward and their differences were compared and analyzed.

The current study is an extension of Tang et al. (2001), Tang (2002) and Tang and Hsieh (2002), in which we will further explore the impact of atmospheric nonlinearities on the ENSO in the framework of the predictability. A core issue addressed in this study is the optimal growth of the uncertainties in the sea surface temperature (SST). Through this study we expect to answer some interesting questions such as (1) where is the most important initial SST located for predicting tropical SST? (2) whether there are differences or not for the answers of (1) between the NHCM and LHCM?, and how large are the differences? (3) do the atmospheric nonlinearities suppress or enhance the growth of perturbations or instabilities? It has been of interest to explore the ENSO predictability using different dynamical models through singular vector (SV) analysis that characterizes the optimal growth of the initial condition errors (e.g., Blumenthal 1991; Xue et al. 1994, 1997a, b; Chen et al. 1997; Thompson 1998; Moore and Kleeman 1996, 1997a, b; Fan et al. 2000; Tang et al. 2006). It was found that while leading vectors (optimal patterns) are less varied, the corresponding leading singular values are highly dependent on models, optimization periods, and initial times. For example, the optimal pattern of perturbation is mainly characterized by an east–west dipole in the entire tropical Pacific basin in many models including Zebiak and Cane model (ZC) (1987), Battisti's model (1988), Thompson's model (1998), and Moore and Kleeman's model (1997a, b). In these works, SVs were calculated using either the forward integration method or the tangent-linear and adjoint method. The former approach is to approximately estimate the full tangent linear matrix of a model for computing SVs via SV decomposition (SVD) method. In order to obtain the approximate tangent linear matrix, the model is required to repeatedly integrate forward, each generated by perturbing a small amount to one initial state (e.g., Lorenz 1965; Chen et al. 1997). When the dimension of model states is large, this approach is very expensive. Alternatively the latter is an elegant algorithm and cheaply produces accurate SVs, but it is difficult and complex to construct tangent linear and adjoint models.

In this paper we will first construct tangent linear and adjoint models for two HCMs, one with linear statistical atmosphere coupled with an oceanic model (LHCM) and the other with a nonlinear NN atmospheric model coupled with the same oceanic model (NHCM). Further, we perform the SV analyses for both models. The optimization periods of 3, 6 and 9 months and two kinds of initial conditions, which are derived from the annual cycle and the real ENSO cycle, will be, respectively, considered for the SV analyses. The paper is organized as follows: the coupled atmosphere–ocean models are described in Sect. 2; in Sect. 3 we will introduce the construction of tangent linear and adjoint models, and the method of SV. We present the results on the optimal error growth as a function of the seasonal cycle and as a function of actual ENSO cycle in Sects. 4, and 5. Finally, a summary and conclusion are presented in Sect. 6.

2 Model description

2.1 Ocean model

The ocean model used in the study is an intermediate complexity model identical to that in Tang et al. (2001; Tang 2002). It covers the tropical Pacific Ocean 30°N–30°S in latitude and 123°E–69°W in longitude with a horizontal resolution of 1.5° × 1.5°. The time step is 2 h. The model allows for exchanges of mass, momentum and heat at each layer interface by a parameterization of entrainment. The boundaries are closed with free slip conditions. The prognostic variables of the model are temperature, layer thickness and velocity.

2.2 Atmosphere models

The atmospheric models are empirical statistic models. One is a traditional LR widely used in HCMs (e.g., Barnett et al. 1993) and the other is a nonlinear regression model, a NN (Hsieh and Tang 1998). The wind stress is constructed using ocean states as predictors. Here we will briefly introduce two kinds of atmosphere models used in this study. The details of the ocean model and atmospheric models can be found in Tang et al. (2001) and Tang (2002).

An EOF (empirical orthogonal function) analysis was first applied to each dataset to extract the predictors and predictands. The oceanic predictor field $T(x,t)$, and the predictand $\tau(x,t)$, the zonal or meridional component of the wind stress, were expressed by EOF analysis as

$$T(x,t) = \sum_n \alpha_n(t) e_n(x) \quad \tau(x,t) = \sum_n \beta_n(t) f_n(x)$$

where n is the mode number and the seasonal cycle has been removed for both fields prior to the EOF analysis. We used the first three EOF modes of oceanic variables T as predictors, and the first three EOF modes of zonal or meridional wind stress as predictands, in constructing both the linear and nonlinear models. The LR model is similar to

that of Barnett et al. (1993), which assumed that the wind stress anomalies τ were a linear response to T, namely, β_n was obtained from α_n via a simple linear relationship.

For the nonlinear regression model, a feed-forward NN that is a non-parametric statistical model was used to construct nonlinear relationships among different data. A common NN model configuration is to place a layer of "hidden neurons" between the input and output variables. The value of the jth hidden neuron is

$$y_j = \tanh\left(\sum_i w_{ij}x_i + b_j\right),$$

where x_i is the ith input, w_{ij} the weight parameters and b_j the bias parameters. The output neuron is given by

$$z = \sum_j \tilde{w}_j y_j + \tilde{b}.$$

A cost function or objective function

$$J = \left\langle (z - z_{\text{obs}})^2 \right\rangle,$$

measures the mean square error between the model output z and the observed data z_{obs}. The parameters w_{ij}, $\tilde{w}_j$, b_j, $\tilde{b}$ are estimated by minimizing the cost function iteratively. The procedure, known as network training, yields the optimal parameters for the network when we find the extremum of the defined scalar cost function by the quasi-Newtonian method or the steepest decent method.

The three input neurons were the first three EOF time series α_n (t), and the single output neuron was the zonal or meridional wind stress EOF time series. There was no time lag between the predictors and the predictand. The prognostic variable is the wind stress in the atmospheric model.

3 The construction of tangent linear and adjoint models and computation of SV

3.1 The construction of tangent linear and adjoint models

The tangent linear and adjoint models were developed for both HCMs. Denoting by the $\boldsymbol{x}$ model state vector, the model equations of motion can then be represented symbolically as:

$$\frac{\partial \boldsymbol{x}}{\partial t} = \boldsymbol{m}(\boldsymbol{x}), \tag{1}$$

where $\boldsymbol{m}(\boldsymbol{x})$ represents the model dynamical operator, which is in general nonlinear. The tangent linear form was derived by considering small perturbations X to $\boldsymbol{x}$, and performing a first-order Taylor expansion to Eq. 1 yields:

$$\frac{\partial \boldsymbol{X}}{\partial t} = \frac{\partial \boldsymbol{m}(\boldsymbol{x})}{\partial \boldsymbol{x}}\Big|_{x_b} \boldsymbol{X} = \boldsymbol{L}\boldsymbol{X}, \tag{2}$$

where $\boldsymbol{x}_b$ is an equilibrium of Eq. 1, and

$$\boldsymbol{L} = \frac{\partial \boldsymbol{m}(\boldsymbol{x})}{\partial \boldsymbol{x}}|_{x_b}$$

is the Jacobian matrix. The adjoint model is derived by considering the inner-product of Eq. 2 with an arbitrary vector $\mathbf{X}^*$, represented symbolically as:

$$-\frac{\partial \boldsymbol{X}^*}{\partial t} = \boldsymbol{L}^*\boldsymbol{X}^*. \tag{3}$$

Using the definition of the adjoint operator $\mathbf{L}^*$:

$$(\boldsymbol{X}^*, \boldsymbol{L}\boldsymbol{X}) = (\boldsymbol{L}^*\boldsymbol{X}^*, \boldsymbol{X}), \tag{4}$$

$\boldsymbol{L}^*$ can be obtained by Euclidean inner product. In fact,

$$\boldsymbol{L}^* = \boldsymbol{L}^T, \tag{5}$$

where $\boldsymbol{L}^{\mathrm{T}}$ is the transpose of matrix $\boldsymbol{L}$ (Bouttier and Coutier 1999).

Several automatic differentiation and adjoint compilers have been developed to generate TLMs (Tangent Linear Model) and AMs (Adjoint Model), such as TAMC (Giering and Kaminski 1998) and TAPENADE (http://www.TAPENADE.inria.fr:8080/TAPENADE/index.jsp). In this study, TAPENADE was used to develop TLM and AM codes for both HCMs. Given a source computer program that computes a differentiable mathematical function $\boldsymbol{F}$, TAPENADE builds a new source program that computes some of the derivatives of $\boldsymbol{F}$, specifically directional derivatives ("tangent mode") and gradients ("adjoint mode").

The TLM is verified by the method suggested by Navon et al. (1992). A scalar d is defined as below

$$d = \frac{\|\boldsymbol{m}[\boldsymbol{x}(t) + \alpha\boldsymbol{X}(t)] - \boldsymbol{m}[\boldsymbol{x}(t)]\|}{\|\alpha\boldsymbol{L}\boldsymbol{X}(t)\|}, \tag{6}$$

where $\boldsymbol{X}(t)$ is the perturbation based on $\boldsymbol{x}(t)$, and α is a scale value, used to control the amplitude of perturbation. A TLM will be correct only and if only the d is close to 1 at the computer precision when α approaches a very small amount. The amount of the α depends on the norm of $\boldsymbol{X}$ and the operators $\boldsymbol{L}$ and $\boldsymbol{m}$.

3.2 The computation of SVs

The algorithm to compute the SVs based on the TLM and AM can be found in literature (e.g., Moore et al. 1996; Li et al. 2005). Here we will present it briefly. The solution to

Eq. 2 for the perturbation $\boldsymbol{X}$ ($\boldsymbol{X}$ is SST perturbations in this study) is given by

$$\boldsymbol{X}(t+\delta t) = \boldsymbol{M}(t+\delta t, t)\boldsymbol{X}(t), \tag{7}$$

where $\boldsymbol{X}(t+\delta t)$ and $\boldsymbol{X}(t)$ are the perturbation at time $t + \delta t$ and t separately. δt is the time interval. $\boldsymbol{M}(t+\delta t,\ t)$ is the propagator from time t to $t + \delta t$ and

$$\boldsymbol{M}(t+\delta t) = exp\left(\int_t^{t+\delta t} \boldsymbol{L}dt\right).$$

The amplification of the perturbation vector over time period (δt) is

$$\lambda^2 = \frac{\|\boldsymbol{X}(t+\delta t)\|^2}{\|\boldsymbol{X}(t)\|^2} = \frac{\langle \boldsymbol{PX}(t+\delta t), \boldsymbol{WPX}(t+\delta t)\rangle}{\langle \boldsymbol{DP}_0\boldsymbol{X}(t), \boldsymbol{P}_0\boldsymbol{X}(t)\rangle} = \frac{\langle \boldsymbol{PMX}(t), \boldsymbol{WMPX}(t)\rangle}{\langle \boldsymbol{DP}_0\boldsymbol{X}(t), \boldsymbol{P}_0\boldsymbol{X}(t)\rangle} = \frac{\langle \boldsymbol{X}(t), \boldsymbol{M}^*\boldsymbol{P}^*\boldsymbol{WMPX}(t)\rangle}{\langle \boldsymbol{DP}_0\boldsymbol{X}(t), \boldsymbol{P}_0\boldsymbol{X}(\boldsymbol{t})\rangle}, \tag{8}$$

where $\boldsymbol{M}^*$ is the adjoint of tangent linear matrix. $\boldsymbol{W}$ and $\boldsymbol{D}$ denote weighting matrices at time $t + \delta t$ and t, respectively; they are positive definite operators and define the norms that are used to measure the errors at the final and initial time. They determine the properties by which the SVs are constrained at final and initial time. The $\boldsymbol{P}(\boldsymbol{P}_0)$ is the projection operator for the final (initial) time. They are used to choose the variables or regions of interest for SVs computation. Normally the $\boldsymbol{P}$ ($\boldsymbol{P}_0$) sets the state vector to zero outside a prescribed area at optimization time (Barkmeijer et al. 1998) or exclude some variables at the final (the initial) time. Consequently, the growth of SVs outside the target area or some variables is not taken into account in the actual computation. $\boldsymbol{P}^*$ and $\boldsymbol{P}_0^*$ are the transpose matrix of $\boldsymbol{P}$ and $\boldsymbol{P}_0$, respectively. In this study, $\boldsymbol{P}$ and $\boldsymbol{P}_0$ are set to exclude all the other variables but the SST at the final and initial conditions.

The scalar λ defined by Eq. 8 is the ratio between the $\boldsymbol{W}$-norm of $\boldsymbol{X}$ at final time and the $\boldsymbol{D}$-norm of $\boldsymbol{X}$ at initial time. Notice that the norm at initial and final time may differ. The leading SV has the property that it maximizes the λ, and the second SV maximizes the λ in the space $\boldsymbol{D}$-orthogonal to the leading SV, and so forth. In this way, one obtains a set of SVs which are $\boldsymbol{D}$-orthogonal at initial time and $\boldsymbol{W}$-orthogonal at final time. Notice that the solutions of maximizing Eq. 8 also satisfy the following generalized eigenvalue problem,

$$\boldsymbol{M}^*\boldsymbol{P}^*\boldsymbol{WPMX} = \lambda^2\boldsymbol{P}_0^*\boldsymbol{DP}_0X. \tag{9}$$

In practice, one can only compute a small number of SVs compared with a huge number of model dimension. Since the matrix $\boldsymbol{M}^*\boldsymbol{P}^*\boldsymbol{WP}\mathbf{M}$ is symmetric, a Lanczos algorithm (Golub and van Loan 1989) can be used to find select eigenvectors and eigenvalues. In this study, we use the ARPACK (ARnoldi PACKage) software package (Lehoucq et al. 1998) that was developed from the Lanczos algorithm to solve the singular value problems.

When we refer to the SV, without qualification we mean the right SV or equivalently the initial pattern of the optimal perturbation. Corresponding to the initial pattern, the final pattern can be written as (Chen et al. 1997):

$$\boldsymbol{M}(t+\delta t, t)\boldsymbol{E_i} = \lambda_i\boldsymbol{F_i}, \tag{10}$$

where $\boldsymbol{E}_i$ is the ith SV, $\boldsymbol{F}_i$ is the ith final pattern, and λ_I is the ith singular value. From Eq. 10 it is clear that λ_iF_i is obtained by integrating the TLM which is assigned the initial field $\boldsymbol{E}_i$.

3.3 The error norm and perturbation of variables

Singular vectors defined in Eq. 9 depend on the form of matrices $\boldsymbol{D,W,P}$ and $\boldsymbol{P}_0$. The forms often used include total energy norm (Moore and Kleeman 1996), the model error variance (Fan et al. 2000), individual model-grid-point variances (Xue et al. 1997a), and L_2-norm (Chen et al. 1997; Tang et al. 2006) etc. For simplicity, L_2-norm is chosen for both HCMs in this study. It means here that the error defined is with respect to the whole tropical Pacific model domain.

The uncertainty in many variables can lead to prediction errors in a realistic coupled model. It is of interest to investigate which variables must be determined most accurately at forecast initialization time to produce the best SST forecast. Often the answer is model-dependent. Using an intermediate complexity coupled model and energy norm, Moore and Kleeman (1996) found that thermocline information was much more important than SST for SST prediction. Xue et al. (1997a) obtained similar conclusions when using the ZC model. On the other hand, using a hybrid model very similar to the model used in this study, Fan et al. (2000) concluded that the initial information of both the SST field and the thermocline field are equally important for SST prediction in the tropical Pacific. Thompson (1998) derived a similar conclusion using a different intermediate complexity coupled model. Recently Tang et al. (2006) also found in a fully coupled GCM that the perturbation in SST can lead to faster error growth than in subsurface temperatures. In this study, we will focus on the optimal perturbations of SST prediction due to the initial uncertainties in SST itself, since the atmospheric models used here are empirical statistical relationship between SSTA and wind stress anomaly, thus the perturbation on SST can directly transfer to the coupling system via wind stress.

4 Singular vectors starting from the climatological annual cycle

In this section, we explore the optimal perturbations of ENSO prediction under the initial conditions of the climatological annual cycle. First, we ran both HCMs for 20 years, and derived the climatological annual cycle from the last ten year's model outputs. The resultant climatological cycle is then used as the initial conditions to perform SVs analysis. We will focus on the differences of the optimal perturbations between the LHCM and NHCM in optimization periods of 3, 6 and 9 months.

4.1 The comparisons of the first singular values of HCMs

Displayed in Fig. 1 is the singular-value spectrum for the both HCMs at the optimization period of 6 months. As can be seen, the first singular value (FSV) is larger than twice the second singular value. Therefore FSV characterizes the major properties of the error growth of tropical SST prediction due to uncertainties in initial conditions of SST. This is also true for other optimization periods. Therefore we only focus on the FSV and the corresponding SV in following discussions.

The LHCM FSVs for the optimization period of 3, 6, and 9 months are plotted in solid lines in Fig. 2 as a function of calendar months. As can be seen, the LHCM's FSV varies little with the start time for the 3-month optimization period but have seasonal variations for longer optimization periods. The start time that generates the extreme FSV in the LHCM varies with the optimization periods. For the 6-month optimization period, the maximum and minimum FSV in the LHCM appears, respectively, at the start time of summer and fall/winter. For the 9-month optimization period, however, the LHCM has the maximum and minimum FSV at the start time of spring/fall and the summer, respectively. This indicates that when some initial conditions lead to large error growth of prediction in the LHCM for the leading time of 6 months, the same initial conditions might lead to small error growth for the leading time of 9 months. This explains well the variation of model skills with lead times in some hybrid coupled models (HCMs), in which the prediction skills do not decrease smoothly with lead times (e.g., Tang et al. 2003). In contrast, the prediction skill is probably higher at the 9-month lead time than at the 6-month lead time. One probable reason for this is that the linear statistical atmosphere used in the LHCM fails to represent well the error growth property for the longer period when the nonlinearity's role might be important. The importance of atmospheric nonlinearities can be suggested by the variation of error growth in the NHCM which has a considerable consistency for different optimization periods: i.e., the maximum error growth rate appearing in spring and fall and the minimum error growth rate appearing at summer for both 6- and 9-month optimization periods (shown in dashed line in Fig. 2).

Another significant difference between the LHCM and the NHCM in Fig. 2 is that the NHCM FSV is always smaller than the counterpart of LHCM for all cases. This is due mainly to the fact that the LHCM has a stronger coupling process than the NHCM. Tang and Hsieh (2001) studied in details the differences between the LHCM and

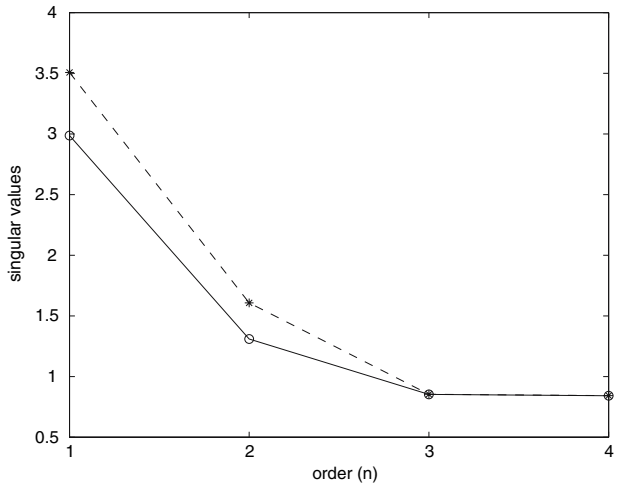

Fig. 1 The singular value spectrum starting in June at the optimization time of 6 months for the NHCM (*solid line*) and the LHCM (*dashed line*)

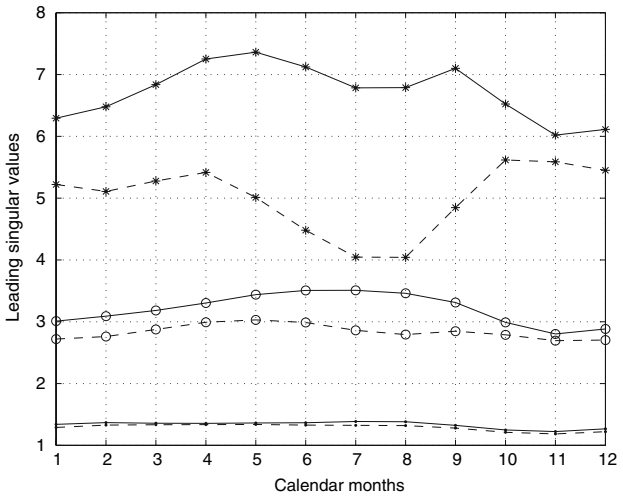

Fig. 2 The FSV (fastest growth rate of perturbation) of Nino3 SSTA prediction based on the seasonal background at the optimization time of *3*-(*dots*), *6*-(*circles*), and *9*-(*asterisks*) months as a function of start time, for the LHCM (*solid line* superimposed over *dot*, *circle*, and *asterisk*) and for the NHCM (*dashed line* superimposed over *dot*, *circle*, and *asterisk*)

NHCM and found that the LHCM produces stronger trade wind anomalies. Moore and Kleeman (1996) also found that the FSV varies approximately in proportion to coupling strength. Figure 3 shows the differences of FSVs between the LHCM and the NHCM for three different optimization periods. From Fig. 3, several interesting points can be concluded: (1) the differences amplify with the increase of the optimization period, suggesting that the impact of nonlinearity on the prediction error growth increases with the lead times of prediction; (2) Fig. 3 explains reasonably well why the NHCM has better prediction skills than the LHCM for long lead times, as shown in Tang et al. (2003); (3) the largest and smallest differences between the NHCM and LHCM occur, respectively, at summer and fall, with the values of 2.74 and 0.43 for the 9-month optimization period and 0.66 and 0.11 for the 6-month optimization period. The largest difference of error growth between the two models occurs in the summer from which the coupled models will start to integrate for 6 and 9 months. So the models will go through summer, fall or winter. This difference of the FSVs reflects the difference of the two models' uncertainty growths in those seasons.

4.2 The comparisons of SVs

The examination of the first SV (SV1, i.e., the initial pattern leading to the optimal perturbations) indicates that it is neither sensitive to the length of the optimization period, and nor to the start time of the optimization period, in contrast to FSV. Also the patterns of SV1 in the LHCM and in the NHCM are very similar. Figures 4a, b, 5a, b, and 6a, b illustrate the SV1 starting from July for 3, 6 and 9 month optimization period, respectively. As shown in these figures, SV1 is characterized by a central west–east dipole spanning over the entire tropical Pacific for all cases. Such spatial structure of SV1 also appears in some other atmosphere-ocean models such as Chen et al. (1997), Xue et al. (1997a), etc.

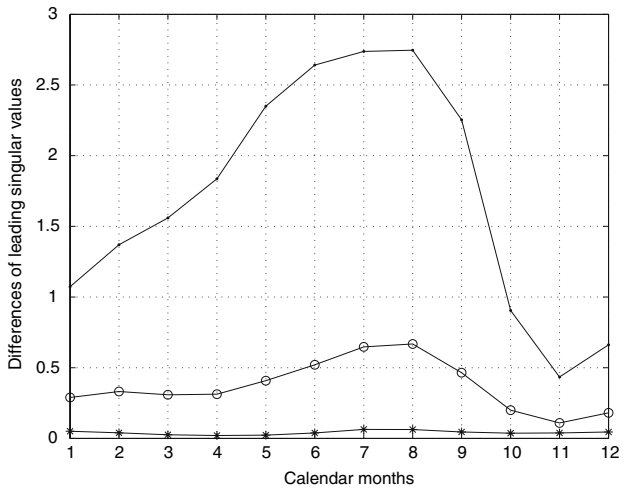

Fig. 3 The differences of FSV at 3-(*dots*), 6-(*circles*), and 9-(*asterisks*) month optimization period between the LHCM and NHCM, as a function of calendar months

It is interesting to compare the SV1 in both HCMs with that in other ENSO coupled models such as Chen et al. (1997), Xue et al. (1997a), Thompson (1998), Moore et al. (1997a), Fan et al. (2000), and Penland et al. (1995). In these coupled models, there are two kinds of atmosphere models used: dynamical atmospheric models (e.g., Chen et al. 1997; Xue et al. 1997a; Thompson 1998; Moore and Kleeman 1996), and linear statistical atmospheric models (e.g., Fan et al. 2000; Penland et al. 1995). In particular, Chen et al. (1997), Xue et al. (1997a) and Thompson (1998) (referred to as CXT hereafter) used different versions of ZC model (1987). Despite the differences in physical and dynamic processes in these coupled models, their SVs have a common feature, i.e., the optimal initial and final pattern have a large-scale structure in the tropical Pacific and the SV1 is not sensitive to the initial time and the length of optimization period. However, the details in the spatial structure of SV1 seem model-dependent. While the SV1 in CXT models has a dipole structure spanning over the tropical Pacific, its strong signals locate in the east-central equatorial Pacific. The SV1 in Moore and Kleeman (1996) is mainly confined to the central and western Pacific. Penland et al. (1995), using a linear Markov model derived from the observed SSTs, found the major signals of SV1 present in the southeastern Pacific. Fan et al. (2000) and Penland et al. (1995) found that the SV1 has positive anomalies in both the eastern and western Pacific, which are different from that in Moore and Kleeman (1997a, b), CXT and both HCMs where there is a negative anomaly in the central Pacific.

The differences of SV1 among these coupled models reflect different physical and dynamical processes. Moore and Kleeman (1997a, b) and CXT used dynamical atmospheric models, and found that the atmospheric heating dominates the structure of SV1. In CXT models, atmospheric heating occurs through surface evaporative anomalies and latent heating that occurs when the wind field is convergent. This latent heating occurs primarily over the east-central and south–west Pacific, which was thought to be probably responsible for large signals of SV1 in the east-central equatorial Pacific. The atmospheric heating used by Moore and Kleeman (1997a) occurs through direct thermal forcing induced by SSTA, and through latent heating in anomalous deep penetrative convection that is induced warm SSTs in the western tropical Pacific where SST exceeds 28°C and is high enough for such convection to occur. Therefore the SV1 in Moore and Kleeman (1997a) is mainly confined to the

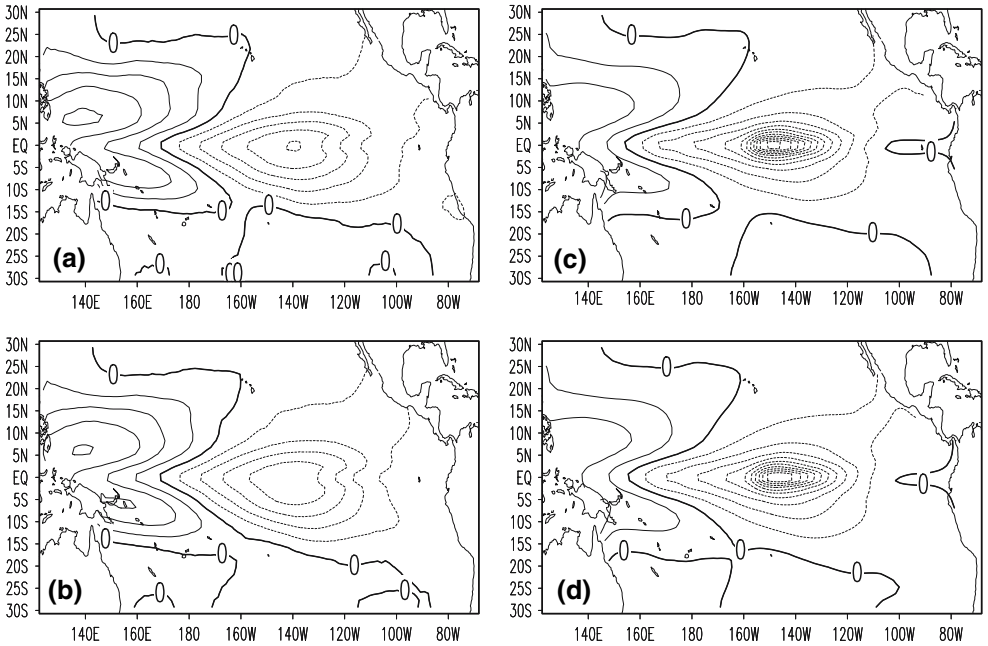

Fig. 4 The first singular vector (SV1) and the corresponding final pattern starting in July at optimization time 3 month. **a**, **b** Represent SV1 of the LHCM and the NHCM. **c**, **d** The final patterns corresponding to the SV1 pattern **a**, **b**. The contour interval is 0.01°C. The *solid lines* indicate positive values and the *dotted lines* indicate negative values

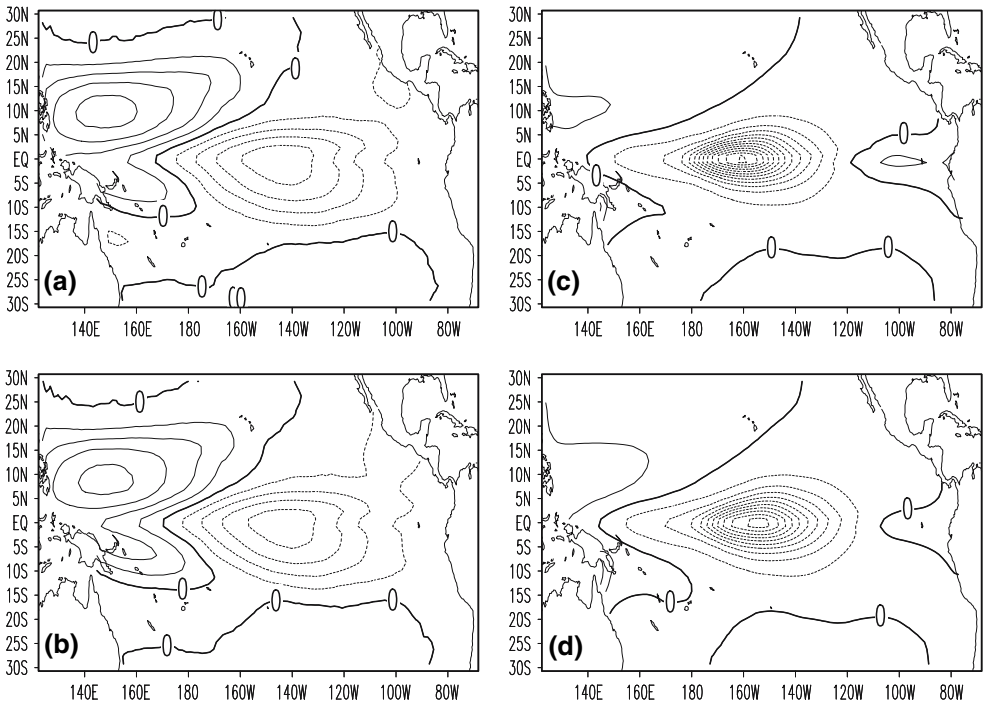

Fig. 5 Same with Fig. 4 but at 6-month optimization time

central and western Pacific. In contrast to the dynamic atmospheric models which mainly respond to local SST, statistical atmospheric models can generate remote wind stress response to the SSTA in the entire central Pacific. Therefore there are large negative and positive anomalies in the central-western tropical Pacific in Fan et al. (2000), Penland and Sardeshmukh (1995), and both HCM models. The strong signals in the central-western tropical Pacific in

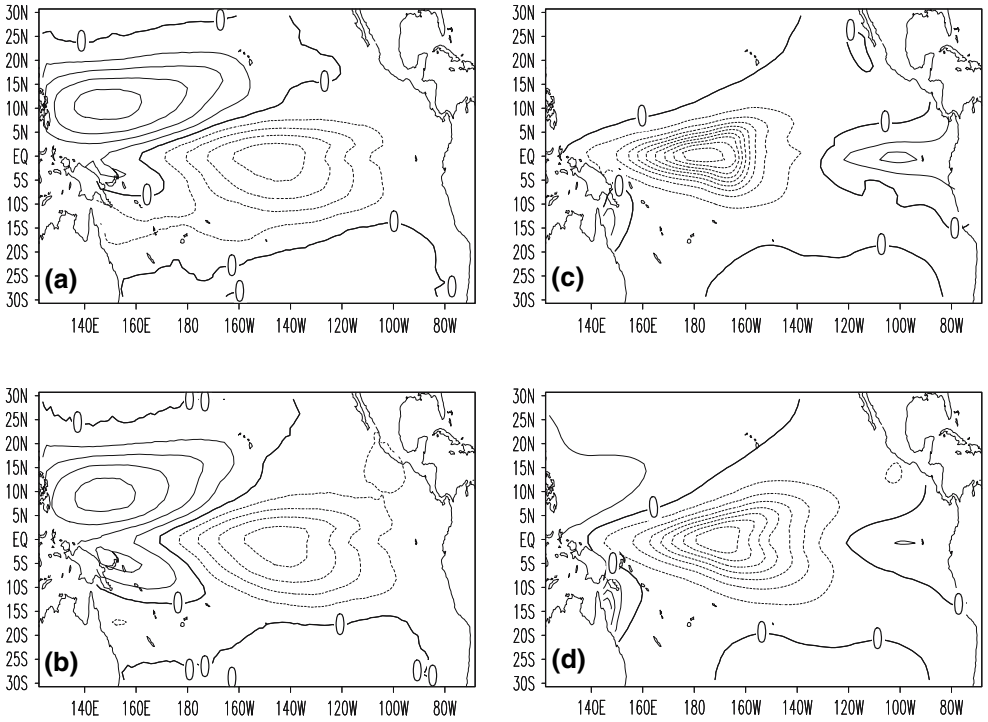

Fig. 6 Same with Fig. 4 but at 9-month optimization time

SV1 are usually absent in these coupled models with dynamical atmosphere component. However, compared with positive anomalies covered in the whole equatorial Pacific in Fan et al. (2000) and Penland and Sardeshmukh (1995), both HCMs show a west–east dipole pattern over the equatorial Pacific.

Like SV1, the final pattern is also very similar to each other between the LHCM and the NHCM, as shown in Figs. 4c, d, 5c, d, and 6c, d. The large SST anomalies in the final pattern always lie to the west of the large SV1 anomalies of the east, suggesting a westward propagation of SSTA anomalies during the optimization period. With the increase of the optimization period, the westward shift is more apparent. Also, the westward shift of SST anomalies is more significant in the LHCM than in the NHCM, which is consistent with the findings in Tang and Hsieh (2001) where the westward propagation of SST anomalies is stronger and extends farther west in the LHCM than the NHCM.

5 Singular vectors starting from the actual ENSO cycle during 1980 to 1999

In this section, we will present the SVs with the actual ENSO cycle, i.e., the initial conditions used to calculate SV are from the actual ENSO variability from January 1980 to December 1999. The actual ENSO variability is obtained by running the ocean model forced by Florida State University (FSU) wind stress (Goldberg and O'Brien 1981). It has been found that the simulated SSTA is in a good agreement with the observed SSTA over the equatorial central and eastern Pacific (Tang et al. 2001). For the consideration of computational cost, we only perform SV analyses every 3 months, starting at the first day of January, April, July and October, respectively. Since the FSV is much larger than the second singular value in all cases, as in Sect. 4, we limit the following discussion to the FSV and the corresponding initial/final optimal patterns.

Figure 7 shows the variation of FSV for both HCMs and the Niño3 SSTA index. There are several apparent features in Fig. 7: (1) the FSV of the LHCM is always larger than those of the NHCM for all cases, which can be explained using the same arguments as in Sect. 4.1; (2) there are strong interannual signals in the FSV of both HCMs.

Figure 7 also shows that for the NHCM the FSV usually has local minima at the peak phase of ENSO episodes and relatively large values at the neutral states, indicating the peak phase of ENSO often leading to smaller error growth. This is interesting since it nicely explains a recent finding in ENSO predictability study that the predictions of stronger ENSO events are more reliable and skillful (Tang et al. 2005). Cai et al. (2003) also obtained similar results when they analyzed the error growth rate of the ZC model

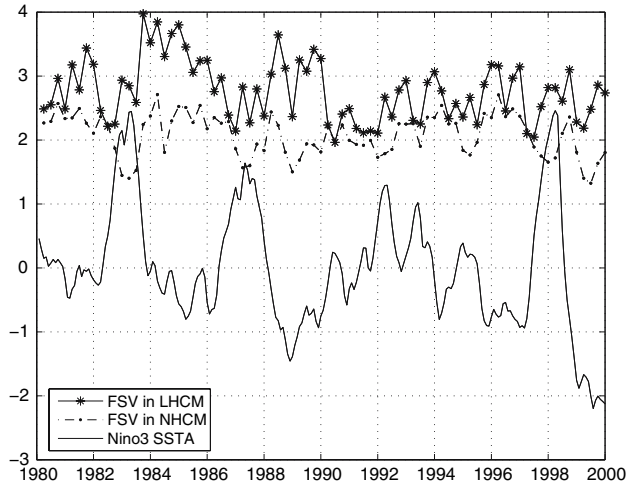

Fig. 7 Time evolution of the first singular value (FSV) in the LHCM (*solid line* with *asterisk*) and the NHCM (*dashed line* with *dot*) at 6-month optimization time, and modeled Nino3 SSTA (*solid line*) forced by FSU wind stress during the period from January 1980 to December 1999

using breeding vector. They argued that this can be explained by the simple delayed oscillator model (Suarez and Schopf 1988), namely,

$$\frac{d\boldsymbol{T}}{dt} = \boldsymbol{T} - \boldsymbol{T}^3 - \alpha \boldsymbol{T}(t - \Delta), \tag{11}$$

where $\boldsymbol{T}$ represents the amplitude of SST anomaly, t is dimensionless time, Δ is the non-dimensional delay time, and α measures the amplitude of the delayed signal relative to the linear and nonlinear feedbacks. The tangent linear model of Eq. 11 can be written as

$$\frac{d\delta\boldsymbol{T}}{dt} = (1 - 3\boldsymbol{T}^2)\delta\boldsymbol{T} - \alpha(t - \Delta)\delta\boldsymbol{T}, \tag{12}$$

where δT is perturbation on T. We could integrate Eq. 12 and obtain

$$\delta\boldsymbol{T}(t) = \delta\boldsymbol{T}(t_0)\mathrm{e}^{-3T^2 t}\beta, \tag{13}$$

where $\beta = e^{\left[(1+\alpha\Delta)t - 1/2\alpha t^2\right]}$, $\delta\boldsymbol{T}(t)$ is uncertainty growth at time t, $\delta\boldsymbol{T}(t)$ is uncertainty at initial time t_0. According to Eq. 13, the ratio $\delta\boldsymbol{T}(t)/\delta\boldsymbol{T}(t_0)$ reaches a minimum value when the background $\boldsymbol{T}$ is one of its two extreme phases, such as the peak El Niño phase or peak La Niña phase; whereas in the neutral state ($\boldsymbol{T} = 0$), the ratio has a larger value.

For the LHCM, most of local minima of the FSV appear at the peak phase of La Niña in Fig. 7. However, in some cases, such as at the weak La Niña events 1985 and 1996, local minima of the FSV does not accordingly appear, indicating that the delayed oscillator mechanism is better represented in the NHCM, further indicating the importance of atmospheric nonlinearities to the error growth.

Unlike the singular value, the spatial structure of SV1 is not sensitive to the optimization period and the start time from which the SV is performed. Figures 8, 9, 10, and 11 show, respectively, the SV1 and corresponding final pattern for four chosen start times: April 1997, October 1997, January 1988 and April 1988. These cases are chosen to represent the SV1 starting from the onset El Niño; the mature El Niño phase; onset La Niña and mature La Niña phase. The optimization time is 6 months in the four cases. As can be seen, the spatial pattern of SV1 is much similar to each other in the four cases, characterized by large anomalies in the equatorial central and western Pacific. The insensitivity of SV1 to the phase of the ENSO cycle was also found in other intermediate coupled models (e.g., Moore and Kleeman 1996; Xue et al. 1997a, b; Chen et al. 1997; Fan et al. 2000), and even in fully coupled GCMs (Tang et al. 2006).

The SV1 derived from the LHCM is in good agreement with that from the NHCM. The striking similarity between them indicates that the spatial structure favoring to the error growth is probably determined by a linear component of atmosphere, and the impact of atmospheric nonlinearity is mainly reflected in the error growth rate.

In contrast to SV1, there are some differences in the final patterns between the LHCM and NHCM due to different error growth rates in the two models. For 1997 El Niño cases, comparing Fig. 8c with d, and Fig. 9c with d reveals that the LHCM has an additional center of error growth, located to the east of dateline, which is absent in the final pattern of the NHCM; whereas for 1988 La Niña cases, the region of maximum error growth in the NHCM is shifted westward by up to 10° in the LHCM (Fig. 11c, d).

The final patterns of LHCM and the NHCM also share some similar features: (1) for 1997 cases, the maximum error growth appears in the eastern tropical Pacific in both HCMs, which resembles the mature mode of ENSO and is similar to other models such as Chen et al. (1997), Xue et al. (1997a), Thompson (1998), Moore and Kleeman (1997a), Fan et al. (2000) and Tang et al. (2006) etc. This maximum center might be due mainly to the fast growth of errors amplified by Kelvin waves. There is also a fast growth region in the western Pacific, which is probably related to the unstable growth of error by Rossby waves; (2) for 1988 La Niña cases, the maximum error growth appears at the central-eastern tropical Pacific first (Fig. 10c, d), and then moves further to the west (Fig. 11c, d).

6 Summary and discussions

In this study, we explored the impact of atmospheric nonlinearities on the optimal growth of the uncertainty in the initial SST. This was performed by comparing and

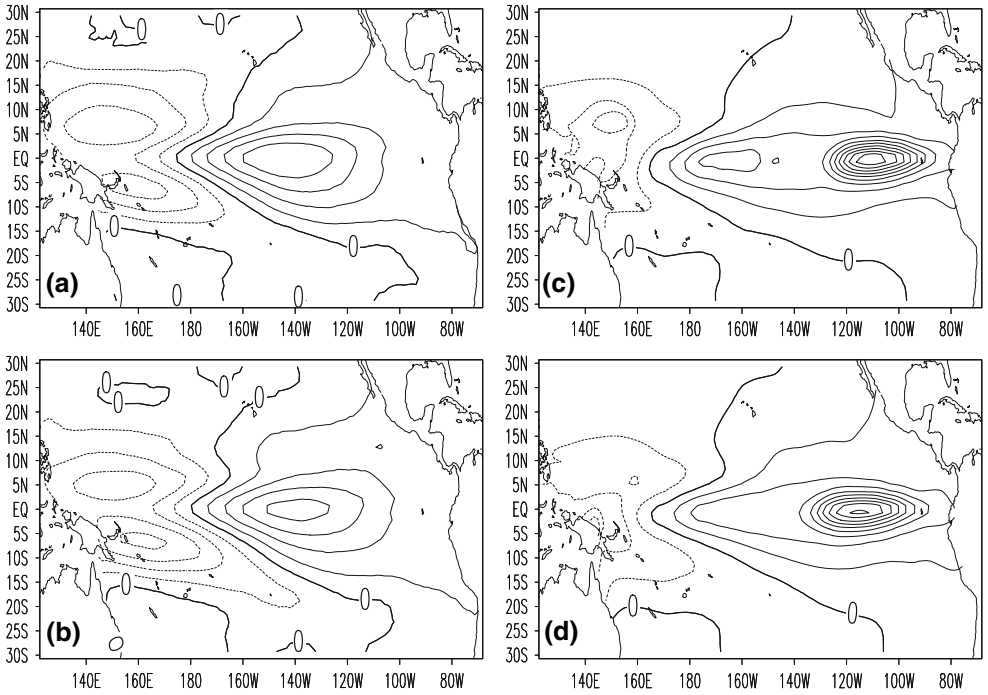

Fig. 8 The SV1 starting at April 1997 in **a** the LHCM and **b** the NHCM. Their corresponding final patterns 6-month later are shown in **c** and **d**. The contour interval is 0.01°C. The *solid lines* indicate positive values and the *dotted lines* indicate negative values

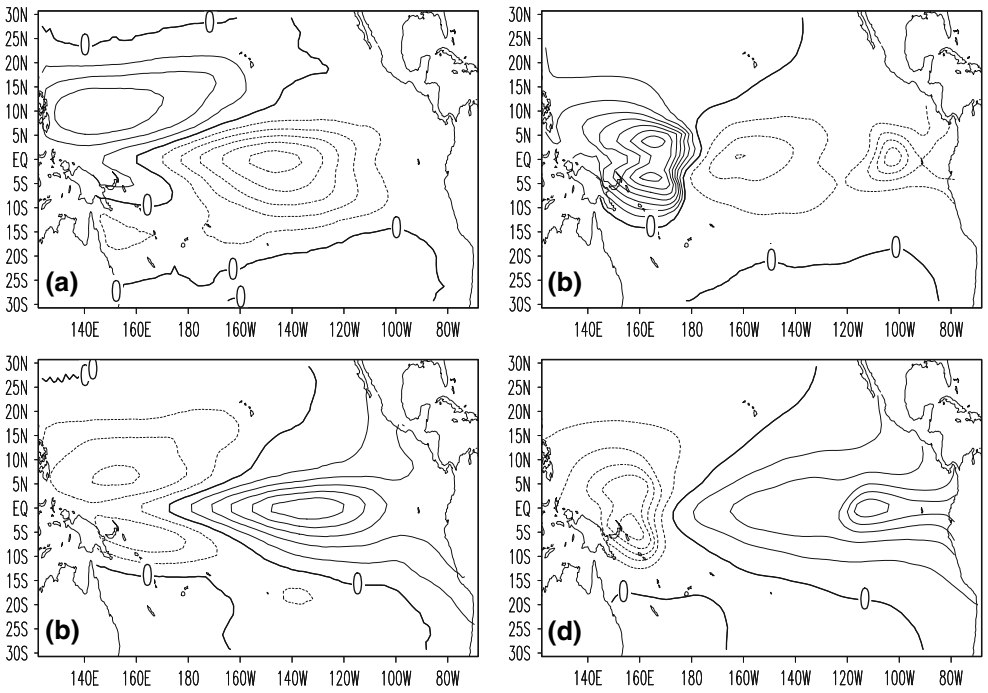

Fig. 9 Same as Fig. 8 but start at October 1997

analyzing SVs of two HCMs, one composed of an intermediate complexity dynamical ocean model coupled with a linear statistical atmospheric model, and the other one with the same ocean model coupled with a nonlinear statistical atmosphere. The tangent linear and adjoint models were first developed for both HCMs, then annual cycle and

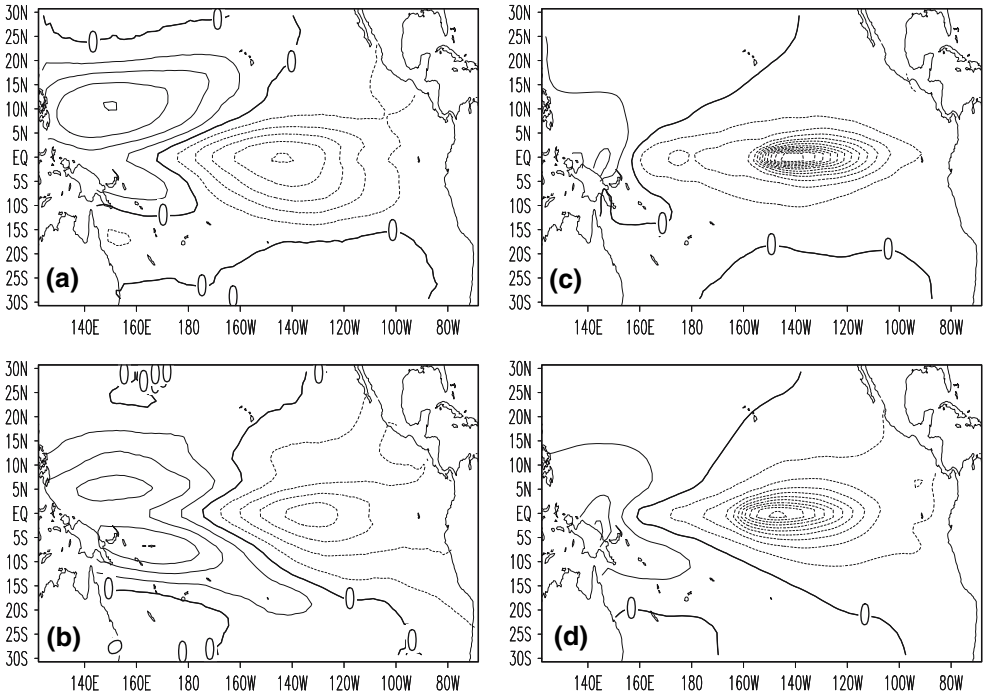

Fig. 10 Same as Fig. 8 but start at January 1988

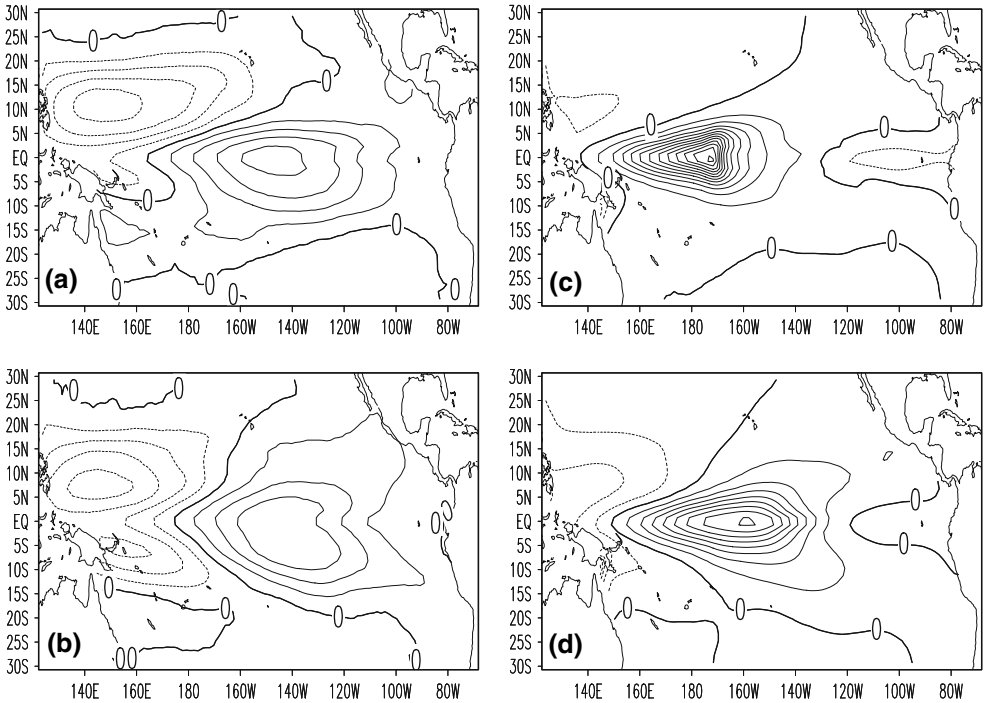

Fig. 11 Same as Fig. 8 but start at April 1988

actual ENSO cycle from 1980 to 1999 were chosen as the initial conditions for SV analysis. The results show that the SVs of both the LHCM and the NHCM share many similar characteristics, including: (1) their error growth is usually dominated by the FSV; (2) the first SV is characterized by a central west–east dipole pattern spanning over the tropical

Pacific; (3) the SV1 is not sensitive to optimization period and start time; (4) the fastest error growth rate is not sensitive to start time for the 3-month optimization period but depends on the start time for the longer optimization period.

The major differences of the SVs and singular values between the LHCM and the NHCM are: (1) the fastest error growth rate in the LHCM is always larger than that in the NHCM, and their difference increases with the increase in optimization time; (2) the largest differences of the fastest error growth rates between the LHCM and the NHCM occur in the summer time when the initial conditions given by the model climatological cycle; (3) The fastest growth rate usually reaches local minima at the peak phase of ENSO in the NHCM, but in the LHCM the fastest growth rate usually has local minima before the peak phase of ENSO; (4) the region of maximum error growth in the NHCM is shifted westward by up to 10° in the LHCM, if SV is calculated from a La Niña phase and has the 6- or 9-month optimization period.

In this study we focused on the comparison of SV between two HCMs and examine their features of singular values and SVs. Therefore an L_2 norm under SST to SST is chosen for simplicity, namely that $\boldsymbol{D}$ and $\boldsymbol{W}$ are identity matrices in formula Eq. 10. It should be noted that SVs and singular values are not unique and depend on the choice of error norm.

The other issue that should be borne in mind is that we only considered the error growth due to uncertainties in SST. While some works show the importance and usefulness of SST in initializing ENSO prediction (e.g., Fan et al. 2000; Tang et al. 2004; Tang and Kleeman 2002; Yuan and Rienecker 2003), other work also found the critical role of subsurface information in ENSO prediction (e.g., Ji et al. 1998). In this study, we did not pay attention to the optimal perturbation due to the uncertainties in such other fields as thermocline depth, and subsurface temperature etc. This is because, besides the importance of SST, this study addresses the comparison of SV between two models, which allowed us to only consider the impact of uncertainties in SST on predictions. On the other hand, the atmospheric models used here are empirical statistical relationships between SSTA and wind stress anomaly, thus the perturbation on SST can directly transfer to the coupling system via wind stress.

An interesting question is how the atmospheric nonlinearities contribute to the SVs since the SVs are computed using linearized models (tangent linear and adjoint model). The impact of atmospheric nonlinearities on SVs can be reflected in two aspects: (1) the tangent linear and adjoint model of a NHCM are different from those of a linear atmosphere; (2) the SVs computation is always with respect to a reference trajectory around which the perturbation is done. In this study, the reference trajectories for both HCMs are generated by the coupled atmosphere-ocean models, so they are different except the initial conditions, which are derived from either a control run that the ocean model is forced by FSU wind stress or a climatology run. It should be noticed that the atmospheric nonlinearities of NHCM impact its reference trajectory. Thus the atmospheric nonlinearities lead to differences in both model linearization and reference trajectories in the SVs analysis.

Acknowledgments This work was supported by Canadian Foundation for Climate and Atmospheric Sciences Grant GR-523 to Y. Tang. XZ wishes to thank Dr. Zhijin Li for his helpful discussions to compute the SVs.

References

An S, Jin FF (2004) Nonlinearity and asymmetry of ENSO. J Clim 17:2399–2412

Barkmeijer J, van Gijzen M, Bouttier F (1998) Singular vectors and estimates of the analysis error covariance matrix. Q J R Meteor Soc 124:1695–1713

Barnett TP, Graham N, Latif M, Pazan S, White W (1993) ENSO and ENSO-related predictability. Part I: prediction of equatorial Pacific sea surface temperature with a hybrid coupled ocean–atmosphere model. J Clim 6:1545–1566

Battisti DS (1988) The dynamics and thermodynamics of a warming event in a coupled tropical atmosphere–ocean model. J Atmos Sci 45:2889–2919

Blumenthal MB (1991) Predictability of a coupled ocean–atmosphere model. J Clim 4:766–784

Bouttier F, Coutier P (1999) Data assimilation concepts and methods. Available from the website http://www.ecmwf.int/newsevents/training/lecture_notes/LN_DA.html

Cai M, Kalnay E, Toth Z (2003) Bred vectors of the Zebiak-Cane model and their application to ENSO predictions. J Clim 16:40–56

Chang P, Li H, Flügel M (1996) Chaotic dynamics versus stochastic process in El Niño-Southern oscillation in coupled ocean–atmosphere models. Physica D 98:301–320

Chen YQ, Battisti DS, Palmer TN, Barsugli J, Sarachik ES (1997) A study of the predictability of tropical Pacific SST in a coupled atmosphere–ocean model using singular vector analysis: the role of the annual cycle and the ENSO cycle. Mon Wea Rev 125:831–845

Chen D, Cane MA, Kaplan A, Zebiak SE, Huang D (2004) Predictability of El Niño in the past 148 years. Nature 428:733–736

Eisenman I, Yu L, Tziperman E (2005) Westerly Wind Bursts: ENSO's tail rather than the dog? J Clim 18:5224–5238

Fan Y, Allen MR, Anderson DLT, Balmaseda MA (2000) How predictability depends on the nature of uncertainty in initial conditions in a coupled model of ENSO. J Clim 13:3298–3313

Gebbie G, Eisenman I, Wittenberg A, Tziperman E (2007) Modulation of Westerly Wind Bursts by sea surface temperature: a semi-stochastic feedback for ENSO. J Atmos Sci (in press)

Giering R, Kaminski T (1998) Recipes for adjoint code construction. ACM Trans Math Softw 24:437–474

Goldberg SD, O'Brien JJ (1981) Time and space variability of tropical Pacific wind stress. Mon Wea Rev 109:1190–1207

Golub GH, Van Loan CF (1989) Matrix computations, 2nd edn. Johns Hopkins University Press, Baltimore

Hsieh WW, Tang B (1998) Applying neural network models to prediction and data analysis in meteorology and oceanography. Bull Am Meteorol Soc 79:1855–1870

Ji M, Behringer D, Leetmaa A (1998) An improved coupled model for ENSO prediction and implications for ocean initialization. Part II: the coupled model. Mon Wea Rev 126:1022–1034

Jin FF, Neelin DJ, Ghil M (1994) El Niño on the devil's staircase: annual subharmonic steps to chaos. Science 264:70–72

Jin FF, An S, Timmermann A, Zhao J (2003) Strong El Niño events and nonlinear dynamical heating. Geophys Res Lett 30:1120. doi:10.1029/2002GL016356

Lehoucq RB, Sorensen DC, Yang C (1998) ARPACK users' guide. SIAM, Philadelphia

Li Z, Navon IM, Hussaini YM (2005) Analysis of the singular vectors of the full-physics FSU global spectral model. Tellus A 57:560–574

Lorenz EN (1965) A study of the predictability of a 28-variable atmospheric model. Tellus 17:321–333

Moore AM, Kleeman R (1996) The dynamics of error growth and predictability in a coupled model of ENSO. Q J R Meteor Soc 122:1405–1446

Moore AM, Kleeman R (1997a) The singular vectors of a coupled ocean–atmosphere model of ENSO. II: sensitivity studies and dynamical interpretation. Q J R Meteor Soc 123:983–1006

Moore AM, Kleeman R (1997b) The singular vectors of a coupled ocean-atmosphere model of ENSO. Part 1: thermodynamics, energetics and error growth. Q J R Meteor Soc 123:953–981

Moore AM, Kleeman R (1999) Stochastic forcing of ENSO by the Intraseasonal Oscillation. J Clim 12:1199–1220

Navon IM, Zou X, Derber J, Sela J (1992) Variational data assimilation with an adiabatic version of the NMC spectral model 120. Mon Wea Rev 7:1433–1446

Penland C, Sardeshmukh P (1995) The optimal growth of tropical sea surface temperature anomalies. J Clim 8:1999–2024

Suarez MJ, Schopf PS (1988) A delayed action oscillator for ENSO. J Atmos Sci 45:3283–3287

Tang Y (2002) Hybrid coupled models of the tropical Pacific—Interannual variability. Clim Dyn 19:331–342

Tang Y, Hsieh WW (2001) Coupling neural networks to incomplete dynamical systems via variational data assimilation. Mon Wea Rev 129:818–834

Tang Y, Hsieh WW (2002) Hybrid coupled models of the tropical Pacific—ENSO prediction. Clim Dyn 19:343–353

Tang Y, Hsieh WW, Tang B, Haines K (2001) A neural network atmospheric model for hybrid coupled modeling. Clim Dyn 17:445–455

Tang Y, Kleeman R, Moore A (2004) SST assimilation experiments in a tropical Pacific Ocean model. J Phys Oceangr 34(3):623–642

Tang Y, Kleeman R, Moore A (2005) On the reliability of ENSO dynamical predictions. J Atmos Sci 62(6):1770–1791

Tang Y, Kleeman R, Miller S (2006) ENSO predictability of a fully coupled GCM model using singular vector analysis. J Clim 19:3361–3377

Thompson CJ (1998) Initial conditions for optimal growth in a coupled ocean–atmosphere model of ENSO. J Atmos Sci 55:537–557

Thompson CJ, Battisti DS (2001) A linear sochastic dynamical model of ENSO. Part II: analysis. J Clim 14:445–66

Tziperman E, Stone L, Cane MA, Jarosh H (1994) El Niño Chaos: overlapping of resonances between the seasonal cycle and the Pacific Ocean–Atmosphere oscillator. Science 264:72–74

Xue Y, Cane MA, Zebiak SE, Blumenthal MB (1994) On the prediction of ENSO–a study with a low-order Markov model. Tellus 46A:512–528

Xue Y, Cane MA, Zebiak SE, Blumenthal MB (1997a) Predictability of a coupled model of ENSO using singular vector analysis. Part I: optimal growth in seasonal background and ENSO cycles. Mon Wea Rev 125:2043–2056

Xue Y, Cane MA, Zebiak SE, Blumenthal MB (1997b) Predictability of a coupled model of ENSO using singular vector analysis. Part II: optimal growth and forecast skill. Mon Wea Rev 125:2057–2073

Yuan D, Rienecker MM (2003) Inverse estimation of sea surface heat flux over the equatorial Pacific Ocean: seasonal cycle. J Geophys Res 108(C8):3247

Zebiak SE, Cane MA (1987) A model El Niño–Southern oscillation. Mon Wea Rev 115:2262–2278